HHS Public Access

Author manuscript

IEEE Trans Biomed Eng. Author manuscript; available in PMC 2018 March 01.

Published in final edited form as:

IEEE Trans Biomed Eng. 2017 March ; 64(3): 715–724. doi:10.1109/TBME.2016.2573682.

A Novel Quantitative 500-MHz Acoustic-microscopy System for Ophthalmologic Tissues

Daniel Rohrbach[1] **[Member, IEEE]**, **Anette Jakob**[2], **Harriet O. Lloyd**[3], **Steffen H. Tretbar**[2] **[Member, IEEE]**, **Ronald H. Silverman**[1,3] **[Senior Member, IEEE]**, and **Jonathan Mamou**[1] **[Senior Member, IEEE]**

[1]Frederic L. Lizzi Center for Biomedical Engineering, Riverside Research, New York, NY 10025 USA

[2]Department Medical Ultrasound, Fraunhofer Institute for Biomedical Engineering IBMT, 66280 Sulzbach, Germany

[3]Department of Ophthalmology, Columbia University Medical Center, New York, New York 10032, USA

Abstract

Objective—This paper describes development of a novel 500-MHz scanning acoustic microscope (SAM) for assessing the mechanical properties of ocular tissues at fine resolution. The mechanical properties of some ocular tissues, such as lamina cribrosa (LC) in the optic nerve head, are believed to play a pivotal role in eye pathogenesis.

Methods—A novel etching technology was used to fabricate silicon-based lens for a 500-MHz transducer. The transducer was tested in a custom designed scanning system on human eyes. Two-dimensional (2D) maps of bulk modulus (K), mass density (ρ) were derived using improved versions of current state-of-the-art signal processing approaches.

Results—The transducer employed a lens radius of 125 μm and had a center frequency of 479 MHz with a −6-dB bandwidth of 264 MHz and a lateral resolution of 4 μm. The LC, Bruch's membrane (BM) at the interface of the retina and choroid, and Bowman's layer (BL) at the interface of the corneal epithelium and stroma, were successfully imaged and resolved. Analysis of the 2D parameter maps revealed average values of LC, BM and BL with KLC = 2.81 ± 0.17; GPa, KBM = 2.89 ± 0.18; GPa, K BL = 2.6 ± 0.09; GPa, ρ LC = 0.96 ± 0.03 g/cm3; ρ BM = 0.97 ± 0.04 g/cm3; ρ BL = 0.98 ± 0.04g/cm3;

Significance—This novel SAM was shown to be capable of measuring mechanical properties of soft biological tissues at microscopic resolution; it currently is the only system that allows Simultaneous measurement of K, ρ, and attenuation in large lateral scales (field area > 9 mm2) and at fine resolutions.

Index Terms

Acoustic microscopy; human eye; 500-MHz ultrasound; mechanical properties

I. Introduction

Over the last four decades, scanning acoustic microscopy (SAM) has become an established imaging modality to characterize acoustical and mechanical properties of hard and soft biological tissues at microscopic resolutions[1]–[3]. SAM typically requires raster scanning tissue samples and uses high frequency ultrasound (i.e., > 50 MHz) to form two-dimensional (2D) images. SAM is well established for non-destructive testing applications with studies developed in the 1970s [1], and the first SAM studies of biological tissues were performed a few years later [4], [5]. Although SAM now is a mature technology, estimating all possible material properties in a single measurement remains a challenging task, particularly at frequencies greater than 300 MHz. SAM studies of soft tissues are more challenging than those involving non-biological materials because of technical and sample-preparation-related difficulties. Nevertheless, SAM has been applied successfully to characterize various soft tissues such as skin, coronary-artery, lymph-node, prostate, tendon, liver, and muscle tissue [3], [6]–[13].

Two primary methods are used to measure acoustical properties of tissues using SAM: surface reflection and through transmission [2], [14]. In through transmission, echo signals are recorded after they pass through thin specimen sections [4], [9], [12], [15] and are reflected from a planar substrate surface. Therefore, echo-signal data acquired in the through transmission approach can be exploited to estimate speed of sound (c), acoustic impedance (Z), and ultrasound attenuation (α) as well as bulk modulus (K) and mass density (ρ), which are directly related to c and Z. [16].

The ability of SAM to estimate acoustic and elastic properties (i.e., K and ρ) of tissues is of particular interest in ophthalmology because abnormal values of mechanical properties are believed to be implicated in several ophthalmic diseases. Therefore, measuring them with microscopic resolution can provide invaluable information regarding the pathogenesis of these diseases. However, very few studies have reported SAM measurements for ocular tissues [4], [16], [17]. Beshtawi *et al.* [17] found a 5 % increase of speed of sound of cross-linked corneal tissue compared to cryosectioned corneas using SAM. Marmor *et al.* [4] found significant variations of acoustic properties of retinal layers. Finally, our group recently demonstrated that tissue mechanical properties at 7-μm resolution significantly differ among layers of murine retinas, indicating that structural changes are manifested in the mechanical properties of tissue at the micron level [16].

This paper focuses on our investigation of three specific regions of the eye to illustrate the value of the 500-MHz SAM system: the lamina cribrosa (LC), Bruch's membrane (BM), and Bowman's layer (BL). The LC is a mesh like plate composed of fine collagen fibers within the optic nerve just below the optic-nerve head. In normal eyes, the LC is approximately 450 μm thick, but in glaucoma, it thins significantly to about 150 μm [18]. The beams of the LC forming the mesh-like structure are about 5–15 μm thick in the normal eye [19]. Changes in the elastic properties of the LC are believed to play a role in glaucoma [20]–[22]. Bruch's membrane, is an acellular, multi-layered structure situated between the vascular choroid and the retinal pigment epithelium. It plays an important role in diffusion of oxygen from the choroid to the retina. BM is known to thicken and become less elastic with

aging [23]–[25]. BL is an approximately 10–15 μm thick basement membrane sandwiched between the corneal epithelium and stroma. Bowman's layer is composed of highly interwoven, small-diameter (24–27 nm), collagen fibrils. In keratoconus (a progressive corneal dystrophy), Bowman's layer demonstrates irregular thinning, fragmentation, and breaks [26], even early in the disease when the stroma is only minimally affected. This suggests that changes in Bowman's layer may represent an early manifestation of the disease process. Early detection of keratoconus is imperative for clinical management.

Characterization of the biomechanical properties of the LC, BM and BL, has heretofore primarily been based on methods such as strip extensiometry [27]–[29], that assess the gross properties of these fine structures. The ability of SAM to assess such properties at a microscopic scale commensurate with the dimensions of the structures of interest, in this case <4 μm, allows us to obtain a greater understanding of the pathogenesis of diseases such as keratoconus, macular degeneration, and glaucoma.

To perform these investigations successfully, an important component of the SAM system is the acoustic lens, which is a key component of the focused ultrasound transducer. The properties and performance of the acoustic lens ultimately determine the quality of the images that the SAM system can produce. In most cases, the acoustic lens consists of a thin piezoelectric zinc oxide (ZnO) film deposited on a sapphire cylinder that has a spherically ground cavity on the opposite side of the ZnO layer [5], [12], [30], [31]. The lens-grinding process is suboptimal in many aspects; it is a single-item production method with low reproducibility and high cost, and it permits only lenses with radii that can be produced using commercially available grinding tools. Another key challenge to overcome is the so called rim echo because the rim around the lens cavity generates an intense unfocused signal, which is received shortly before the focused echo signal and interferes with the echo signals from the sample. To reduce this undesirable effect, lenses with long working distances are typically used; however, because of high attenuation in water at frequencies above 400 MHz, the signal-to-noise ratio (SNR) achieved with long working distance lenses is poor, which makes this approach impractical for very high-frequency SAM systems. Therefore, in this study, we investigated a novel transducerdesign approach using an etching processes to make a 500- MHz transducer with short working distance, no rim-echo issues, and satisfactory SNR.

II. Material and Methods

A. System requirements

To image acoustical properties of LC, Bruch's membrane, and Bowman's layer successfully, a SAM system must meet specific requirements that usually are not available on commercial instruments. These requirements can be separated in three main categories: scanning system requirements, transducer requirements, and ophthalmologic sample requirements. The requirements are summarized in Table 1.

B. Transducer design and realization

Prior to manufacturing the transducer, theoretical calculations and simulations were performed. Specifically, analytical calculation of the lens geometry as described by A. Briggs [14] and simulation of the sound field were conducted to meet the transducer design requirements outlined in Table 1. These simulations were performed with the simulation tool SCALP developed by Fraunhofer to calculate the transient propagation of acoustic waves [32]. Parameters for lens aperture-angle and radius were successively varied to determine the optimal settings. The software takes into account attenuation in water which is very significant at 500 MHz; the attenuation coefficient in water used was 0.23dB/(μm*GHz^2) at 20 °C [14].

The parameters that best fit the transducer requirements outlined above were found to be 125 μm ± 50 μm for the lens radius and 60° for the aperture angle. The corresponding sound field simulation showed a 6-dB depth of field of 31 μm and a 6-dB focal diameter of 3.7 μm.

To produce the desired lens geometry, we opted to use an etching method instead of mechanical grinding. The method was adapted from our previous work [33]. The transducer was fabricated on silicon wafer using photolithography technology. A schematic process flow is shown in Fig. 1 and more details can be found in [33]. Steps (a) to (d) illustrate the isotropic etching of hemispheres inside the wafer by using a mixture of hydrofluoric and nitric acid (HNA). The aperture angle was reduced to values < 90° by dry etching (steps (e) to (h)). The lens was covered with a matching layer of silica (step (i)). A piezo electric ZnO layer with electrodes was sputtered on the wafer back side (steps (j) to (l)). The wafer was separated into single chips which were fixed on a printed circuit board with SMA connector and mounted on stainless steel housing.

The manufactured lens geometry was evaluated with a scanning electron microscope (EVO MA10, Carl Zeiss Microscopy, Germany). The lens radius and aperture angle were then quantified using a 3D confocal profilometer (μscan, Nanofocus, Germany). Then, determination of the −6-dB depth of field, the working distance, the SNR, the center frequency and the −6-dB bandwidth of the transducer using the scanning system described in the next Section was performed. To assess lateral resolution, the transducer was used to image an USAF test target (POG Präzisionsoptik, Gera, Germany).

C. Scanning system

The scanning system was entirely designed at Riverside Research and Fig. 2a and 2b show a photo of the system and its operating block diagram. The device uses a 500-MHz monocycle pulser (GEOZONDAS, Vilnius-09, Lithuania) to excite the ultrasound transducer and radio-frequency (RF) signals were amplified using a 1-GHz bandwidth, 30-dB amplifier (MITEQ, Hauppauge, NY, USA) and digitized at 2.5 GHz using a 12-bit oscilloscope (Teledyne LeCroy, Chestnut Ridge, NY, USA). The specimens were scanned by mounting the microscope slide in an upside down configuration (Fig. 2c) on a three-axis, high-precision scanning stage (Newport, Irvine, CA, USA). The upside down configuration is favorable because it prevent deposition of air bubbles or debris originating from the sample. Scan increment was set to 1 μm and a drop of filtered water was used as coupling medium. To

guarantee that the sample glass slide was perpendicular to the incident beams, long single-line scans (i.e., 6 mm) were acquired along the x-axis and the y-axis. Then, the tilt of the slide was manually corrected and single-line scans repeated until the time of flight of all the signals emanating from the glass-only region were identical. To adjust the tilt, precise micrometers on the tilt stage connected to slide holder were used (Fig. 2)

For comparison purposes, the samples were scanned using the 500-MHz transducer and system, then the same samples were scanned with our established 250-MHz SAM. The 250-MHz SAM was described previously [16] and consists of the same scanning stage and oscilloscope as the 500-MHz system. Transducer excitation was performed using a 300-MHz monocycle pulser (GEOZONDAS, Vilnius-09, Lithuania) and the scan increment was set to 2 μm.

D. Signal-processing and image formation

RF data were saved and processed offline using dedicated signal-processing methods. The implemented methods follow an approach similar to the one described by Hozumi et al. [9]. For measurements on thin sections of tissue attached to a substrate (i.e., microscopy glass plate) two reflected signals are expected in the recorded RF data. The first reflected signal emanates from the water sample interface (front reflection, s_1) and the second reflected signal emanates from the sample-substrate interface (back reflection, s_2). The recorded signal s can be described as a summation of the two signals where s_1 can s_2 can be modelled as a phase shifted and amplitude modified version of a reference signal s_0 with

$$s(t)=s_1(t)+s_2(t), \quad (1)$$

where

$$\begin{aligned} s_1(t)&=ks_0(t-t_1),\\ s_2(t)&=ms_0(t-t_2)*att. \end{aligned} \quad (2)$$

The factors k and m define the amplitudes of the recorded signals. The symbols t_1 and t_2, give the shift in time of the two signals, and the symbolic convolution (*) by att symbolizes the attenuation effects due to the round-trip propagation inside the sample. The reference signal, $s_0(t-t_0)$, was obtained by averaging signals at a location on the slide devoid of tissue. Mapping s into the Fourier domain, normalizing (i.e., dividing) by the Fourier transform of the reference signal, and taking the square of the magnitude yields

$$\hat{S}\left|\frac{FFT\{s_1+s_2\}}{FFT\{s_0\}}\right|^2=\left|\frac{ke^{-j2\pi ft_1}\int s_0(t)e^{-j2\pi ft}dt+me^{-2df\alpha}e^{-j2\pi ft_2}\int s_0(t)e^{-j2\pi ft}dt}{e^{-j2\pi ft_0}\int s_0(t)e^{-j2\pi ft}dt}\right|^2 \quad (3)$$

$$= \left| k e^{-j2\pi f(t_1 - t_0)} + m e^{-2d\alpha f} e^{-j2\pi f(t_2 - t_0)} \right|^2 \quad (4)$$

$$= k^2 + 2km \cdot e^{-2df\alpha} \cdot cos(2\pi f(t_2 - t_1)) + m^2 e^{-4df\alpha}, \quad (5)$$

with t_0 equal the time of flight of the reference signal, f and, α gives the attenuation coefficient in Neper/MHz/cm. It follows that $\hat{S}$ (5) is an oscillatory function which oscillates approximately between $(k - me^{-2d\alpha f})^2$ and $(k + me^{-2d\alpha f})$ if the attenuation in the sample is neglected the frequencies f_{min} and f_{max} at which $\hat{S}$ reaches an extremum can be found by considering the extrema of the cos function, with

$$2\pi f_{min} \cdot (t_2 - t_1) = (2n+1)\pi, n \in \mathbb{N}_0 \quad (6)$$

$$2\pi f_{max} \cdot (t_2 - t_1) = 2n\pi, n \in \mathbb{N}_0 \quad (7)$$

The phase φ of $S(\hat{S} = \left|\dot{S}\right|^2)$ at the maximum points f_{max} can be written as

$$\varphi(\dot{S}) = \varphi(e^{j2\pi f_{max}(t_0 - t_1)}) + \varphi([k + m \cdot cos(2\pi f_{max}(t_2 - t_1)) - m \cdot j \cdot sin(2\pi f_{max}(t_2 - t_1))]). \quad (8)$$

$$= 2\pi f_{max}(t_0 - t_1). + \varphi(k+m) \quad (9)$$

$$= 2\pi f_{max}(t_0 - t_1) \quad (10)$$

Because $\varphi(\dot{S})$ is only defined between -2π and 2π the unwrapped phase $\varphi_u(\dot{S}) = \varphi(\dot{S}) - 2\pi n, n \in \mathbb{Z}$ can be used which yields

$$\varphi_u(\dot{S}) = 2\pi f_{max}(t_0 - t_1) - 2\pi n \quad (11)$$

$$\iff 2\pi f_{max} \frac{2d}{c_0} = \varphi_u(\dot{S}) + 2\pi n \quad (12)$$

If eqn. 11 is substituted into eqn. 8 it can be found that

$$2\pi f_{max}(t_2 - t_1) = 2\pi f_{max}(t_0 - t_1) - \varphi_u(\dot{S}) \quad (13)$$

$$\iff d = \frac{\varphi_u(\dot{S})}{4\pi f_{max}\left(\frac{1}{c_0} - \frac{1}{\hat{c}}\right)} \quad (14)$$

In eqn. 12 and 14 d corresponds to the sample thickness, c_0 to the speed of sound in the coupling medium and $\hat{c}$ to the speed of sound in the specimen. For the minimum locations it can be shown similarly that

$$d = \frac{c_0}{4\pi f_{min}}(\varphi_u(\dot{S}) + \pi(2n-1)) \quad (15)$$

The locations of f_{min} and f_{max} are detected using peak detection algorithms and the n's can be calculated from the estimated periodicity determined by f_{min} and f_{max}. An initial speed of sound $(\hat{c})$ value is then calculated from eqn. (14) as the average value over all d estimates, for each f_{min} and $f_{\max}$.

To derive estimates of the factors k, m and the attenuation coefficient, the forward model of (5) can be fitted to the normalized, measured spectra, but the optimization can be cumbersome and the value of m is not used at the moment. Therefore, to estimate α directly from the normalized spectrum (5), we used a dichotomy method based on simple algebraic considerations. Specifically, at the extrema of $\hat{S}$ (i.e, S_{M1}, S_{M2} and S_{m1}, with $S_{Mi} = (k + me^{-2df_{Mi}\alpha})^2$, $S_{mi} = (k - me^{-2d\alpha f_{mi}})^2$ and with Mi and mi indicating the i'th maximum and minimum, respectively) it can be found that

$$\frac{\sqrt{S_{M2}} - \sqrt{S_{M1}}}{\sqrt{S_{M2}} + \sqrt{S_{m1}}} = \frac{e^{-2\alpha df_{M2}} - e^{-2\alpha df_{M1}}}{e^{-2\alpha df_{M2}} + e^{-2\alpha df_{m1}}}. \quad (16)$$

α was therefore estimated iteratively from (16). Note, that at least three extrema are required for (16). A similar term can be found for the combination of two minima and one maximum. The values of k and m are then found from two maxima and the estimated α using (5).

In the above calculations, initial speed of sound $(\hat{c})$ was estimated by neglecting the effect of the attenuation on the location of the extrema of $\hat{S}$. However, the attenuation will shift the locations of f_{min} and $f_{\max}$. Therefore, the estimated α value found using (16) was used to mitigate attenuation effects and permit the final estimation of c (and d).

Finally, the acoustic impedance (Z_s) of the sample was estimated from the amplitude (k) of the first signal and the amplitude of the reference signal from first principles using

$$Z_s = \frac{Z_w r_{ref} + \frac{k}{k_{ref}} Z_w}{r_{ref} - \frac{k}{k_{ref}}} \quad (17)$$

where r_{ref} is the reflection coefficient of the reference signal yielding

$$r_{ref} = \frac{Z_{ref} - Z_w}{Z_{ref} + Z_w}, \quad (18)$$

In. (17) and (18) Z_w and Z_{ref} are the known acoustic impedances of water and substrate, respectively.

Parameter (Z, c, and α) estimations were performed independently on each individual RF signal yielding 2D maps of acoustic properties of tissues (speed of sound, acoustic impedance, acoustic attenuation) as well as derived mechanical properties such as mass density ($\rho = Z/c$, in g/cm^3) and bulk modulus ($K = c \cdot Z$, in GPa) [14]. In a final step, the reconstructed parameter maps were de-noised using a median filter of 3×3 μm^2

E. Ophthalmologic samples

Whole human donor eyes (n=3) with no history of ocular disease were obtained from the North Carolina Eye Bank (Winston-Salem, NC, USA and processed in accordance with the provisions of the Declaration of Helsinki for research involving human tissue. Eyes deemed unsuitable for tissue donation were immersed in Excalibur's Fixative solution (Excalibur Pathology, Inc., Norman, OK), paraffin embedded, and serially sectioned. 5-μm sections were cut in transverse planes incorporating the optic nerve head (ONH) for SAM, and then processed for subsequent staining with hematoxyloin and eosin (H&E) and imaging by light microscopy.

F. Imaging protocol

The 5-μm sections used for SAM imaging were first deparaffinized and rehydrated in series of Histoclear ethanol (100%, 75%) and saline (each 2 × 5 min). Before scanning, samples were washed in deionized and degassed water. Then, the slides were mounted on the SAM system in the upside down configuration (Fig. 2c) and raster scanned.

G. Statistical analysis and image analysis

Regions of interests (ROIs) were specified manually based on co-registered histology images to derive means and standard derivations of the acoustic parameters of the different tissues. Co-registration between acoustic and light microscopy images was performed using the amplitude images. The amplitude images were generated from the maximum of the envelope signals (i.e., the Hilbert transform of s). For most soft-tissue applications, the maximum amplitude corresponds to the second reflection (i.e., s_2) and, therefore, contains mixed information about acoustic impedance and attenuation within the sample (as well as thickness). Nevertheless, the amplitude image can be obtained very rapidly, and while they

cannot be used for quantitative analysis, they provide an easy means to localize interesting features in the SAM images for quantitative analysis using the parameter images. To separate the tissue region from the surrounding glass plate-only region a threshold was manually selected based on the histogram of the amplitude images.

Differences between different tissue types were evaluated using one-way ANOVA and post hoc Tukey Kramer multiple comparison test. All statistical analysis, image and signal processing was implemented using MATLAB (The MathWorks Inc., Natick, MA, USA)

III. Results

A. Transducer characterization

Photographs of the assembled transducer are shown in Fig. 4a and 4b. Fig. 4c shows a scanning electron image of the transducer lens. The surface inside the lens is smooth whereas the lens rim has a rougher surface. The lens ground is situated above the circumjacent rim. The profilometer showed that the lens radius was 125 μm. Fig. 3 shows the pulse-echo response obtained at room temperature (i.e., 23 °C) from a glass substrate placed at the focus using the SAM system at Riverside Research. The center frequency was found to be 479 MHz with a 6-dB bandwidth extending from 317 MHz to 581 MHz (i.e., a fractional bandwidth of 55%). In addition, the SNR was found to be 35 dB.

This fabrication method also successfully moved the rim echo away from the focal echo. In fact, the rim echo signal (not shown in Fig. 3) arrives later in time than the focal echo and both signals were well separated. The working distance of the lens was found to be 90 μm. The 6-dB depth of field (DOF) was 30 μm (Fig. 3c). The transducer successfully imaged separate lines on an USAF test target, which were 3.9-μm thick with an interline space of 3.9 μm (Fig. 4d). Thinner closer lines potentially could be resolved.

In conclusion, the results presented in this section clearly confirm that we have met all the transducer requirements shown in Table 1

B. Scanning-system characterization

The system allows measuring a total scanning area of 3*3 mm^2 in less than 40 min. For example, Fig. 5 which shows a SAM image of the optic nerve with a total area of about 1.9 mm^2 took approximately 13 minutes to acquire. The Newport motor stages easily permitted a scan increment of 1 μm. The bandwidth of 1 GHz, sampling frequency of 2.5 GHz and a bit depth of 12 bits were provided by the Lecroy oscilloscope permitted to successfully digitize the signals with adequate SNR and without aliasing artifacts. In conclusion, all necessary design requirements outlined in Table I are met by the SAM device.

C. Quantitative images of ocular-tissue samples

Fig. 5 shows co-registered images from light microscopy after H&E staining (Fig. 5a), SAM amplitude images (Fig. 5b), speed of sound (Fig. 5c), and acoustic impedance (Fig. 5d). The resolution of the system and tissue acoustic contrast are sufficient to visualize the optic nerve sheath, LC and nerve bundles in the optic nerve, the sclera, choroid, retinal nerve fiber layer and retinal substructure, including the pigment epithelium and Bruch’s membrane.

Quantitative analyses yielded the material properties of BM and LC and are summarized in Table 1

Fig. 6 and 7 show comparative images obtained using the 500-MHz and the 250-MHz SAM systems, respectively. Fig. 7 depicts the LC region of the optic nerve, where nerve fiber bundles pass between septa in a porous connective tissue mesh to reach the retina. While the LC is discernable at 250 MHz (arrows in Fig. 7-d), far greater detail in depiction of nerve bundles and connective tissue are seen at the higher frequency (arrows in Fig. 7-b). Similarly, peripapillary retinal layers seen in Fig. 6-d (arrows) obtained using the 250-MHz SAM more clearly depicted at in Fig. 6a–b (arrows) obtained using the 500-MHz SAM.

SAM images of the cornea are shown in Fig. 8. The resolution of the 500-MHz transducer is sufficient to resolve epithelium, stroma, and Bowman's layer. Also, cellular structures are visible in the amplitude and acoustic impedance image. The epithelium shows three different layers with statistically ($p<0.05$, ANOVA) different acoustic impedances. A thin layer (i.e., approximately 5 μm) with low acoustic impedance and speed of sound (Z=1.6±0.02 MRayl, c=1636±24 m/s) but high attenuation (α=7.6±2.8 dB/MHz/cm) in the posterior region, followed by a thicker layer (i.e., approximately 30 μm) with high impedance and speed of sound (Z=1.63±0.04 MRayl, c=1688±0.27) and a last layer (i.e., approximately 18 μm) with low impedance and attenuation values (Z=1.58±0.03 MRayl, c=1652±0.31, α=3.8 dB/MHz/cm). Bowman's layer is clearly visible in the amplitude image and showed significantly ($p<0.05$, ANOVA) lower α (3.1±1.8 dB/MHz/cm), Z (1.61±0.05 MRayl) and c (1632±34 m/s) when compared to other layers. Descemet's membrane had significantly larger bulk modulus (i.e. K=3±0.26 GPa, $p<0.05$) than any other corneal tissue (not shown in Fig. 8). Average acoustical properties of Stroma were c=1651±37 m/s, Z=1.63±0.05 MRayl and α=3.9±2.8 dB/MHz/cm.

IV. Discussion

The results presented in this study demonstrate that the complete SAM system is working successfully. The transducer met design requirements and quantitative images of acoustic properties of human ophthalmologic tissues were obtained with a resolution better than 4 μm.

The parameter-estimation methods presented in Sec. D were successful in providing reliable estimates of the acoustic properties of ophthalmologic tissues. Improvements in current estimation methods were also outlined to provide all acoustic parameters to be estimated simultaneously and to better handle high attenuation occurring at 500 MHz. Nevertheless, several studies are currently ongoing to improve robustness and properly quantify bias and variances of the estimators. The approach presented in Sec. D assumes the existence of only two echo signals and will almost always fail if more than two echo signals exists; additional echo signals could originate from fold in the tissues or even just from noise. Therefore, we are currently developing signal-processing methods which can handle more than two signals, and still provide reliable estimates. In another investigation we are studying the use of m in Eqn. 2 and 4, as outlined in Sec. D. Currently m is not used; however, based on first principles, m can be used to characterize non-linear attenuation. For example, instead of

assuming a linear frequency dependence, we can use m to estimate the exponent of the frequency-dependent attenuation, thereby providing a new quantitative tissue parameter.

Although the SAM system met all the design requirements of Table 1, several improvements are currently under investigation. For example, the next iteration of the system will use fast linear actuator motors with step sizes of 100 nm. We will quickly acquire oversampled data and average 10 adjacent signals to increase SNR. Such improvements will reduce the scan time by a factor of approximately 5 and increase the SNR by approximately 20 dB (under white noise assumption). Another feature we are adding to our SAM system is coded "chirp" signals. In the past, we have been successful in using chirp approaches to increase SNR, penetration depth, and contrast-to-noise ratio for 20- and 40-MHz ultrasound imaging [34]–[37]. For SAM, we propose to use a slightly different approach using customized chirps to enhance the bandwidth of the echo signals in addition to their SNR. This approach was previously used successfully at low frequencies [38]–[40]. The increased bandwidth will provide more-robust estimation by permitting easier separation of s_1 and s_2.

The transducer was fabricated on silicon wafer using photolithography technology. Silicon acoustic lenses have been reported Hashimoto et al. [38], but our innovative approach permits the repeatable realization of lenses with radii between 75 μm and 135 μm and with an aperture angle of 60°. The method also allows shorter working distances with decreased rim echoes and better SNR. The aperture angle can be adapted in a separate dry-etching step to any required value. So, the realized aperture angle of 60° can be changed easily to other values to reach either better lateral resolution or longer depth of field as required. Higher-frequency transducers can be realized with the same technology by using thinner ZnO layers. The dry etching of the rim allows shorter working distances with decreased rim echoes and with a better signal to noise ratio. Compared to the grinding technology, the etching eliminates the need for precision grinding tools. Also, the wafer-based processing allows high reproducibility and the option of low-cost batch processing.

These initial results obtained on ocular tissue samples demonstrate that the SAM system can provide quantitative properties of ocular tissues believed to be associated with a wide range of diseases. However, focus of this paper was the 500-MHz system design, development, and testing. The actual property values obtained in this study must be viewed with caution because only three samples were investigated simply to demonstrate the feasibility of measuring properties of ocular tissues at a microscopic scale. A comprehensive study involving more samples is underway to establish a database of tissue mechanical properties. Furthermore, the samples were obtained from fixed and paraffin-embedded, eye-bank eyes, and those treatments are likely to have altered the mechanical properties of the examined tissues. For example, in the cornea, fixation leads to cross linking of the collagen fibers [17]. In fact, the speed of sound values found in this study of the cornea (i.e., 1651±37 m/s) matches well the values for cross-linked corneas measured at 761 MHz (i.e., 1672.5 m/s) by Beshtawi et al. [17]. The same study also found a speed of sound of 1584 m/s for untreated corneas.

Following successful demonstration of the 500-MHz SAM system on paraffin-embedded samples, we have initiated studies using snap-frozen cryo-sectioned samples to derive more-

realistic estimates of tissue properties at microscopic resolutions. Nevertheless, this initial study demonstrates that ocular tissues show a significant variation of material properties for different tissue types. This is expected because the eye is, in its simplest form, a sphere with positive internal pressure, and the biomechanical properties of structural elements of the ocular wall play a role in several ocular diseases. In keratoconus, the cornea undergoes progressive bulging and assumes a conical shape. In axial myopia, the sclera stretches, resulting in an elongated eyeball and altered scleral properties were reported in high myopia and straphyloma [42], [43]. In glaucoma, the optic nerve undergoes excavation and damage as the lamina cribrosa undergoes elastic deformation, with intraocular pressure being a major risk factor. The biomechanical properties of the sclera and lamina cribrosa may play a role in glaucoma development [44], [45]. Alterations in the elastic properties of Bruch's membrane may be associated with AMD [46].

This study demonstrates that SAM has the potential to provide unique data to understand these disease processes better. Current methods for biomechanical assessment, such as strip extensiometry only measure bulk properties of relatively large tissue samples, which is not a suitable means for assessing elastic properties at the microscopic scale, e.g., assessment of the LC in the optic nerve or Bowman's layer in the cornea. In this report, we demonstrated resolution and contrast that are sufficient to characterize the cornea, retina, optic nerve and their respective components. In addition, our results demonstrated that the 500-MHz SAM system provides far better images of these structures than the 250-MHz SAM system. Therefore, the 500-MHz SAM system offers a unique means to investigate biomechanical changes associated with eye diseases such as keratoconus, myopia and glaucoma.

Conclusions

This study presents a novel SAM capable of measuring mechanical properties of soft biological tissues at microscopic resolution. To the best of our knowledge, no system exists that allows simultaneously measuring attenuation, bulk modulus, and mass density, in large lateral scales (> 9 mm^2) and at fine resolutions (~4 μm) as presented in this work. In addition, our methods also provide a novel signal-processing framework for better parameter estimation in highly-attenuating conditions. Finally, although this study utilized ocular tissues, the 500-MHz SAM clearly can be used to assess the properties of other types of tissues when requirements such as those outlined in Table 1 exist.

Acknowledgments

The work is supported in part by NIH grant EB R21EB016117 awarded to Riverside Research (JM) and by an unrestricted grant awarded to the Department of Ophthalmology of the Columbia University Medical Center by Research to Prevent Blindness. We thank Daniel Gross for his technical support and assistance with the SAM. We are grateful to Albert Chung for his dedicated help with SAM measurements and analysis.

References

1. Lemons RA. Acoustic microscope—scanning version. Appl Phys Lett. 1974; 24(4):163.
2. Raum K. Microelastic imaging of bone. IEEE Trans Ultrason Ferroelectr Freq Control. Jul; 2008 55(7):1417–1431. [PubMed: 18986931]
3. Daft CMW, Briggs GAD. Wideband acoustic microscopy of tissue. IEEE Trans Ultrason Ferroelectr Freq Control. Mar; 1989 36(2):258–263. [PubMed: 18284976]

4. Marmor MF, Wickramasinghe HK, Lemons RA. Acoustic microscopy of the human retina and pigment epithelium. Invest Ophthalmol Vis Sci. Jul; 1977 16(7):660–666. [PubMed: 873726]
5. Quate CF, Atalar A, Wickramasinghe HK. Acoustic microscopy with mechanical scanning A review. Proc IEEE. 1979; 67(8):1092–1114.
6. Daft CMW. Frequency dependence of tissue attenuation measured by acoustic microscopy. J Acoust Soc Am. 1989; 85(5):2194. [PubMed: 2732391]
7. Daft CMW, Briggs GAD. The elastic microstructure of various tissues. J Acoust Soc Am. 1989; 85(1):416. [PubMed: 2921421]
8. Hattori K, Sano H, Saijo Y, Kita A, Hatori M, Kokubun S, Itoi E. Measurement of soft tissue elasticity in the congenital clubfoot using scanning acoustic microscope. J Pediatr Orthop Part B. Sep; 2007 16(5):357–362.
9. Hozumi N, Yamashita R, Lee C-K, Nagao M, Kobayashi K, Saijo Y, Tanaka M, Tanaka N, Ohtsuki S. Time-frequency analysis for pulse driven ultrasonic microscopy for biological tissue characterization. Ultrasonics. Apr; 2004 42(1–9):717–722. [PubMed: 15047373]
10. Miura K, Nasu H, Yamamoto S. Scanning acoustic microscopy for characterization of neoplastic and inflammatory lesions of lymph nodes. Sci Rep. Feb.2013 3
11. Saijo Y. Multimodal ultrasound microscopy for biomedical imaging. Proc Meet Acoust. Jun.2013 19(1):75010.
12. Saijo Y, Tanaka M, Okawai H, Sasaki H, Nitta SI, Dunn F. Ultrasonic tissue characterization of infarcted myocardium by scanning acoustic microscopy. Ultrasound Med Biol. 1997; 23(1):77–85. [PubMed: 9080620]
13. Irie S, Inoue K, Yoshida K, Mamou J, Kobayashi K, Maruyama H, Yamaguchi T. Speed of sound in diseased liver observed by scanning acoustic microscopy with 80 MHz and 250 MHz. J Acoust Soc Am. Jan; 2016 139(1):512–519. [PubMed: 26827044]
14. Briggs, A. Acoustic microscopy. Oxford: New York: Clarendon Press; Oxford University Press; 1992.
15. Saijo Y, Filho E, Sasaki H, Yambe T, Tanaka M, Hozumi N, Kobayashi K, Okada N. Ultrasonic Tissue Characterization of Atherosclerosis by a Speed-of-Sound Microscanning System. IEEE Trans Ultrason Ferroelectr Freq Control. Aug; 2007 54(8):1571–577. [PubMed: 17703660]
16. Rohrbach D, Lloyd HO, Silverman RH, Mamou J. Fine-resolution maps of acoustic properties at 250 MHz of unstained fixed murine retinal layers. J Acoust Soc Am. May; 2015 137(5):EL381–EL387. [PubMed: 25994737]
17. Beshtawi IM, Akhtar R, Hillarby MC, O'Donnell C, Zhao X, Brahma A, Carley F, Derby B, Radhakrishnan H. Scanning Acoustic Microscopy for Mapping the Microelastic Properties of Human Corneal Tissue. Curr Eye Res. Apr; 2013 38(4):437–444. [PubMed: 23402595]
18. Jonas JB, Berenshtein E, Holbach L. Anatomic relationship between lamina cribrosa, intraocular space, and cerebrospinal fluid space. Invest Ophthalmol Vis Sci. Dec; 2003 44(12):5189–5195. [PubMed: 14638716]
19. Kotecha A, Izadi S, Jeffery G. Age-related changes in the thickness of the human lamina cribrosa. Br J Ophthalmol. Aug; 2006 90(12):1531–1534. [PubMed: 16943226]
20. Braunsmann C, Hammer CM, Rheinlaender J, Kruse FE, Schäffer TE, Schlötzer-Schrehardt U. Evaluation of lamina cribrosa and peripapillary sclera stiffness in pseudoexfoliation and normal eyes by atomic force microscopy. Invest Ophthalmol Vis Sci. 2012; 53(6):2960–2967. [PubMed: 22491409]
21. Kim T-W, Kagemann L, Girard MJA, Strouthidis NG, Sung KR, Leung CK, Schuman JS, Wollstein G. Imaging of the lamina cribrosa in glaucoma: perspectives of pathogenesis and clinical applications. Curr Eye Res. Sep; 2013 38(9):903–909. [PubMed: 23768229]
22. Ritch R, Schlötzer-Schrehardt U. Exfoliation syndrome. Surv Ophthalmol. Feb; 2001 45(4):265–315. [PubMed: 11166342]
23. Marshall J. The 2014 Bowman Lecture-Bowman's and Bruch's: tale of two membranes during the laser revolution. Eye Lond Engl. Jan; 2015 29(1):46–64.
24. Moore DJ, Hussain AA, Marshall J. Age-related variation in the hydraulic conductivity of Bruch's membrane. Invest Ophthalmol Vis Sci. Jun; 1995 36(7):1290–1297. [PubMed: 7775106]

25. Ugarte M, Hussain AA, Marshall J. An experimental study of the elastic properties of the human Bruch's membrane-choroid complex: relevance to ageing. Br J Ophthalmol. May; 2006 90(5): 621–626. [PubMed: 16622094]
26. Ramrattan RS, van der Schaft TL, Mooy CM, de Bruijn WC, Mulder PG, de Jong PT. Morphometric analysis of Bruch's membrane, the choriocapillaris, and the choroid in aging. Invest Ophthalmol Vis Sci. May; 1994 35(6):2857–2864. [PubMed: 8188481]
27. Camras LJ, Stamer WD, Epstein D, Gonzalez P, Yuan F. Circumferential Tensile Stiffness of Glaucomatous Trabecular Meshwork. Investig Opthalmology Vis Sci. Feb.2014 55(2):814.
28. Elsheikh A, Geraghty B, Alhasso D, Knappett J, Campanelli M, Rama P. Regional variation in the biomechanical properties of the human sclera. Exp Eye Res. May; 2010 90(5):624–633. [PubMed: 20219460]
29. Ni S, Yu J, Bao F, Li J, Elsheikh A, Wang Q. Effect of glucose on the stress–strain behavior of ex-vivo rabbit cornea. Exp Eye Res. May; 2011 92(5):353–360. [PubMed: 21329688]
30. Ito Y, Yokosawa K, Sano S, Shinomura R, Sato Y. Thin-film ZnO ultrasonic transducers for tissue characterization. 1996; 1:83–86.
31. Atalar A, Jipson V, Koch R, Quate CF. Acoustic Microscopy with Microwave Frequencies. Annu Rev Mater Sci. Aug; 1979 9(1):255–281.
32. Tylkowski BD. Rechnergestütztes Ultraschall-Phased-Array-Design mittels Punktquellensynthese und Evolutionsstrategie. 1994
33. Jakob A, Weiss EC, Knoll T, Bauerfeld F, Herrmann J, Lemor R. P2E-5 Silicon Based GHz Acoustic Lenses For Time Resolved Acoustic Microscopy. 2007:1605–1608.
34. Mamou J, Ketterling JA, Silverman RH. Chirp-coded excitation imaging with a high-frequency ultrasound annular array. IEEE Trans Ultrason Ferroelectr Freq Control. Feb; 2008 55(2):508–513. [PubMed: 18334358]
35. Mamou J, Aristizábal O, Silverman RH, Ketterling JA, Turnbull DH. High-Frequency Chirp Ultrasound Imaging with an Annular Array for Ophthalmologic and Small-Animal Imaging. Ultrasound Med Biol. Jul; 2009 35(7):1198–1208. [PubMed: 19394754]
36. Silverman RH, Ketterling JA, Mamou J, Lloyd HO, Filoux E, Coleman DJ. Pulse-encoded ultrasound imaging of the vitreous with an annular array. Ophthalmic Surg Lasers Imaging Off J Int Soc Imaging Eye. Feb; 2012 43(1):82–86.
37. Filoux E, Mamou J, Aristizábal O, Ketterling JA. Characterization of the spatial resolution of different high-frequency imaging systems using a novel anechoic-sphere phantom. IEEE Trans Ultrason Ferroelectr Freq Control. May; 2011 58(5):994–1005. [PubMed: 21622055]
38. Oelze ML. Bandwidth and resolution enhancement through pulse compression. IEEE Trans Ultrason Ferroelectr Freq Control. Apr; 2007 54(4):768–781. [PubMed: 17441586]
39. Sanchez JR, Pocci D, Oelze ML. A novel coded excitation scheme to improve spatial and contrast resolution of quantitative ultrasound imaging. IEEE Trans Ultrason Ferroelectr Freq Control. Oct; 2009 56(10):2111–2123. [PubMed: 19942499]
40. Linden P, Sanchez JR, Oelze ML. Small lesion detection with resolution enhancement compression. Ultrason Imaging. Jan; 2010 32(1):16–32. [PubMed: 20690429]
41. Hashimoto H, Tanaka S, Sato K. Silicon acoustic lens for scanning acoustic microscope (SAM). 1991:853–859.
42. McBrien NA, Jobling AI, Gentle A. Biomechanics of the Sclera in Myopia: Extracellular and Cellular Factors. Optom Vis Sci. Jan; 2009 86(1):E23–E30. [PubMed: 19104466]
43. Phillips JR, McBrien NA. Form deprivation myopia: elastic properties of sclera. Ophthalmic Physiol Opt J Br Coll Ophthalmic Opt Optom. Sep; 1995 15(5):357–362.
44. Zeimer, Ran. Biomechanical properties of the optic nerve head. Optic Nerve in Glaucoma, Kugler Publications. 1995:107–121.
45. Sigal IA, Flanagan JG, Ethier CR. Factors influencing optic nerve head biomechanics. Invest Ophthalmol Vis Sci. Nov; 2005 46(11):4189–4199. [PubMed: 16249498]
46. Chong NHV, Keonin J, Luthert PJ, Frennesson CI, Weingeist DM, Wolf RL, Mullins RF, Hageman GS. Decreased thickness and integrity of the macular elastic layer of Bruch's membrane correspond to the distribution of lesions associated with age-related macular degeneration. Am J Pathol. Jan; 2005 166(1):241–251. [PubMed: 15632016]

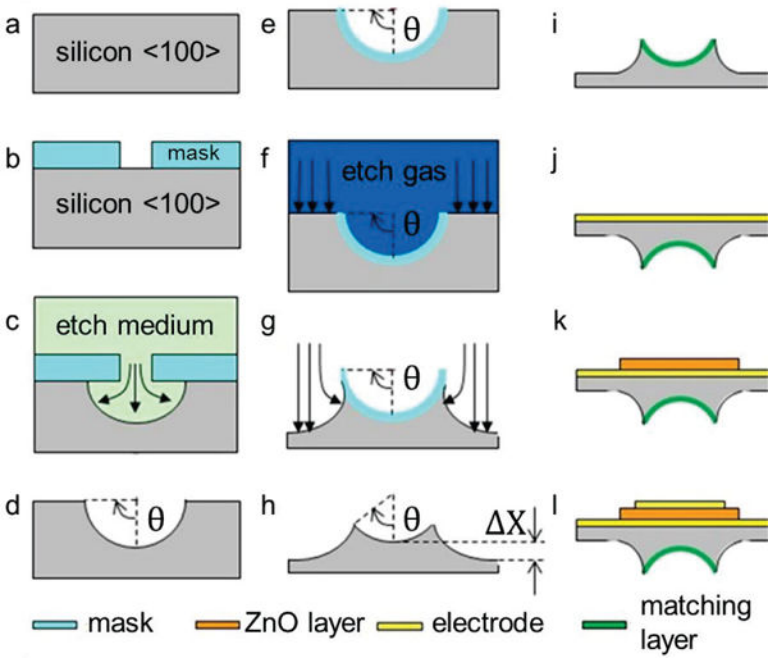

Figure 1.

process flow of the lens fabrication, (a) to (d) isotropic etching of hemispheres inside the wafer by using a mixture of hydrofluoric and nitric acid (HNA). (e) to (h) aperture angle was reduced to values < 90° by dry etching. (i) lens was covered with a matching layer of silica. (j) to (l) piezo electric zinc oxide layer with electrodes was sputtered on the wafer back side.

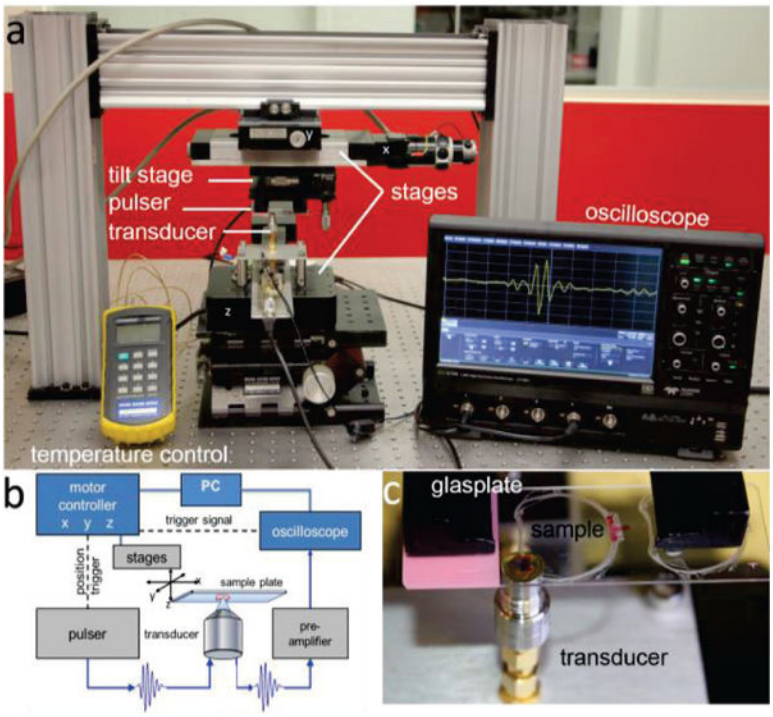

Figure 2.

(a) Photograph of the 500-MHz SAM system. (b) block diagram of working principle (c) magnification of sample mounting and transducer. A eye bank eye sample is visible on the microscopy glass slide.

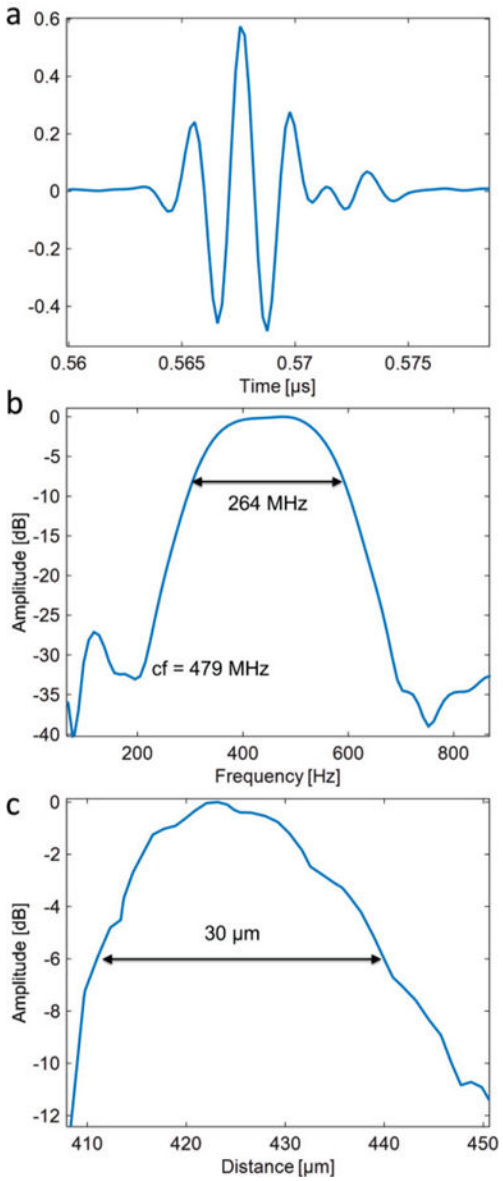

Figure 3.

(a) Time domain signal measured at the focus from a planar reflector (i.e. glass slide). (b) power spectrum of a). (c) Amplitude loss in dB of the echo signal from the glass slide as a function of the distance between the glass slide and the transducer. The 6-dB depth of field was found to be 30 μm

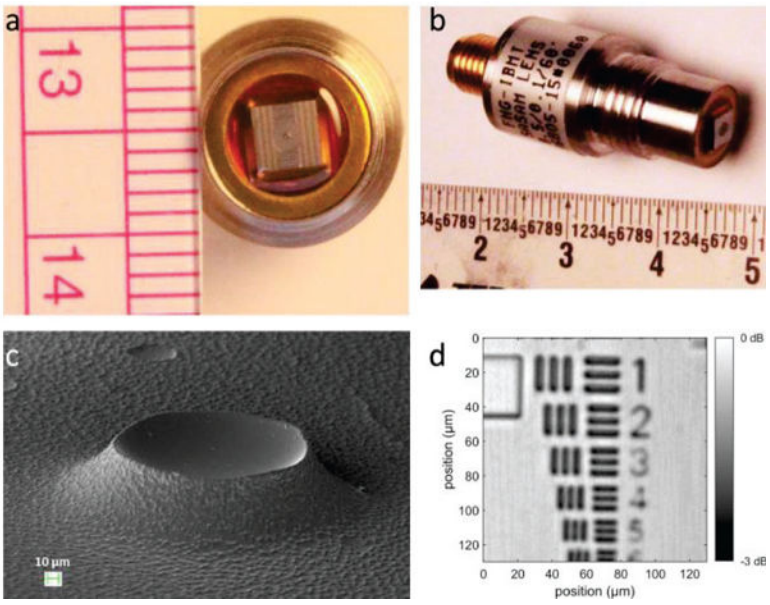

Figure 4.

(a) and (b) shows photographs of the 500 MHz transducer (on both images, distance between largest numbers is 1 cm). (c), Scanning electron image of the lens (EHT=10.00 kV, Mag 750×). (d) SAM amplitude image of an USAF test target to evaluate the lateral resolution of the SAM system. The lines near the “1” (3.9 µm thick and separated by 3.9 µm) were resolved and separated which implies a lateral resolution better than 3.9 µm.

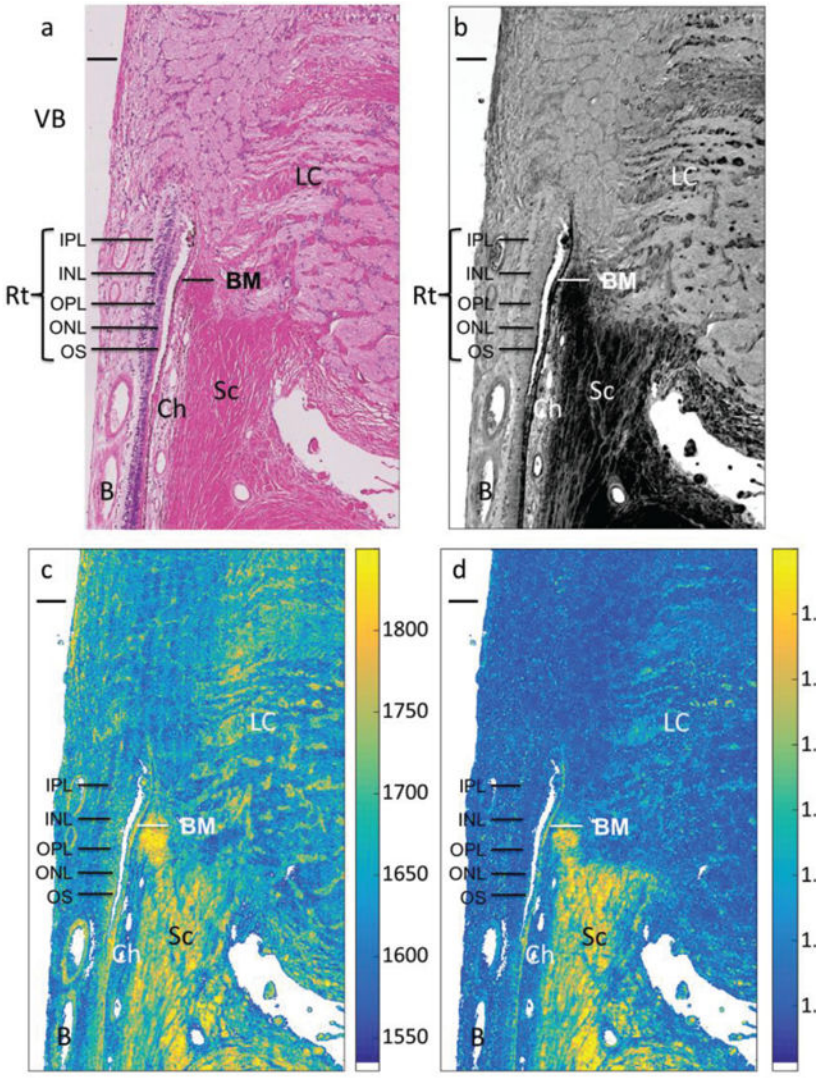

Figure 5.

Images of the optic nerve. (a) H&E light microscopy (b) SAM Amplitude (c) Speed of sound (m/s) (d) Acoustic impedance (MRayl). Abbreviations are retina (Rt), inner plexiform layer (IPL), inner nuclear layer (INL), outer plexiform layer (OPL), outer nuclear layer (ONL), outer segment (OS), vitreous body (VB), optic nerve (ON), blood vessel (B), Bruch's membrane (BM), choroid (Ch), sclera (Sc), lamina cribrosa (LC). Scale bars are 100 μm.

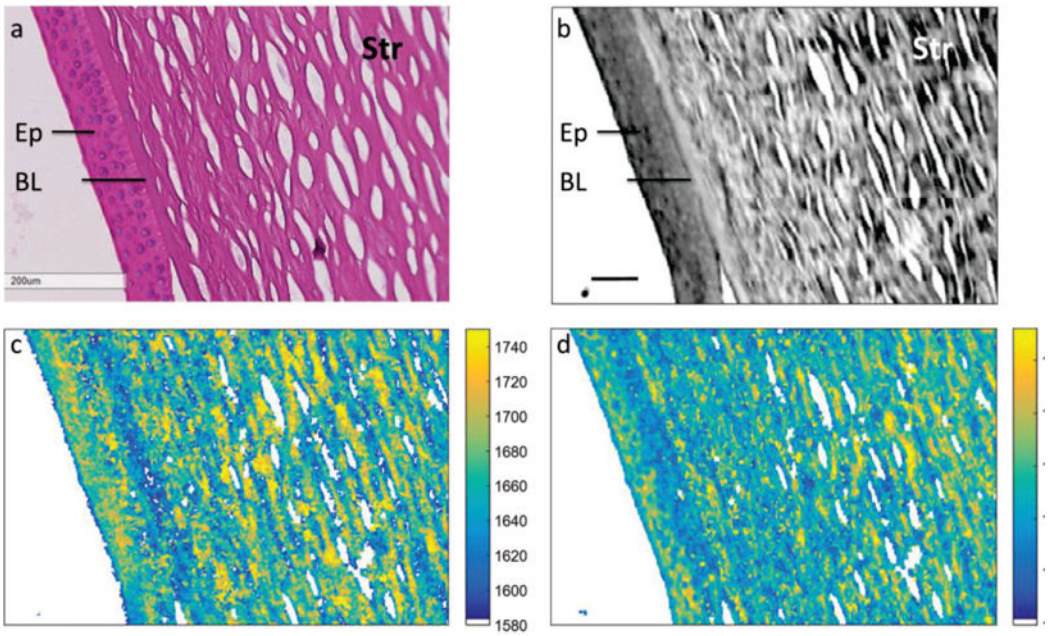

Figure 6.

Images of the cornea. (a) H&E light microscopy, (b) amplitude at 500 MHz, (c) speed of sound and (d) acoustic impedance. Abbreviations are Bowman's layer (BL), epithelium (Ep), stroma (Str). The scale bar is 100 μm.

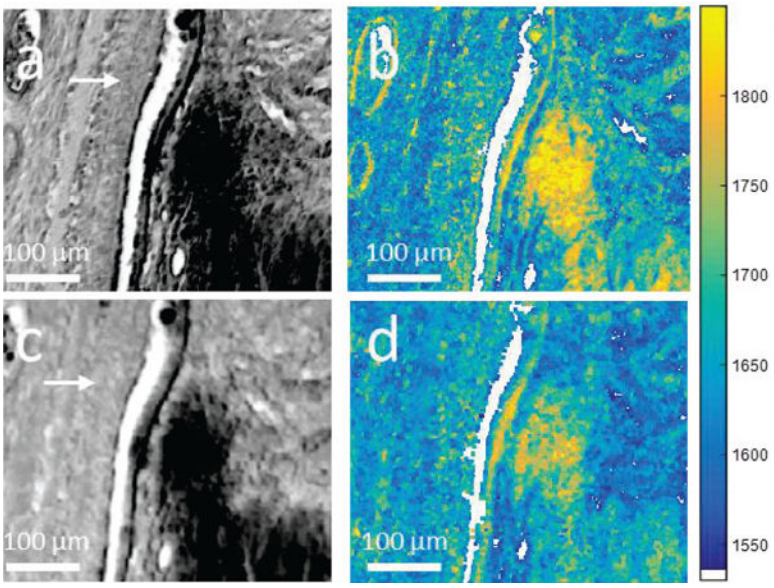

Figure 7.

Comparison of SAM images at sites of Buch's membrane obtained using the 500-MHz system (a–b) and the 250-MHz system. (a) and (c) are SAM amplitude images and (b) and (d) are speed of sound images.

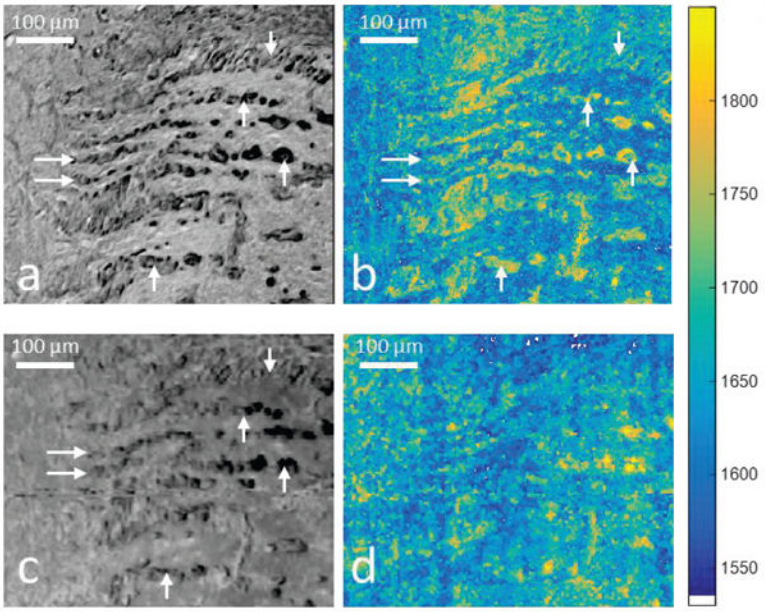

Figure 8.

Comparison of SAM images at sites of the lamina cribrosa obtained using the 500-MHz system (a–b) and the 250-MHz system. (a) and (c) are SAM amplitude images and (b) and (d) are speed of sound images.

Table 1

Design requirements

	Transducer requirements	Purpose	Accomplished
1.	Resolution < 4 μm	Resolve the LC, BM and BL	YES
2.	wd > 80 μm	Use with microscopy slides and avoid rim echo artifacts	YES, 90 μm
3.	cf ~ 500 MHz	Quantify acoustic properties of thin samples	YES, 479 MHz
4.	−6-dB *bw* >250 MHz	Quantify acoustic properties of thin samples	YES 264 MHz
	System requirements		
5.	Large scan area	Eye geometry require assessing the acoustical properties along long distances (i.e., at least 2 mm)	YES, > 3*3 mm^2
6.	Scan increment < 1 μm	Target lateral resolution (i.e., ~4 μm)	YES, motor stages
7.	Sampling frequency > 2 GHz, *bw* > 1 GHz	Sufficient sampling rate for a 500-MHz *cf*	YES, oscilloscope
8.	Bit depth >12 bits	Acoustic signals can have wide dynamic range	YES, oscilloscope
9.	Fast scanning (<15 min for an area 2×2 mm)	Limit potential change in tissue properties	Adequat, 20 min (2×2 mm^2)
	Sample requirements		
10.	Thickness ~ 5μm	Avoid blurry images due to scattering from within the samples or defocusing effects.	YES

abbreviations are center frequency (cf),bandwidth (bw) working distance (wd)

Table 2

TISSUE MATERIAL PROPERTIES

Tissue	K (GPa)	ρM (g/cm^3)	αM (dB/MHz/cm)	c (m/s)	Z (MRayl)
BM	2.89±0.18	0.97±0.04	12.2±9.5	1723±52	1.67±0.07
LC	2.81±0.17	0.96±0.03	8.1±6.6	1714±53	1.64±0.07
BL	2.62±0.17	0.98±0.04	3.1±1.8	1632±34	1.61±0.05

Data presented in mean ± standard deviation